

Chandra Observations and Monte Carlo Simulations of the Grain-Scattered Halo of the Binary X-Ray Pulsar 4U 1538-52

George W. Clark

Center for Space Research, Massachusetts Institute of Technology, Cambridge, MA 02139

ABSTRACT

Properties of the grain-scattered X-ray halo of the eclipsing X-ray binary pulsar 4U 1538-52 are derived from a 25 ksec observation by the *Chandra* X-ray observatory extending from just before its eclipse immersion to near mid-eclipse. Profiles of the observed halo, compiled in two energy ranges, 2 to 4 keV and 4 to 6 keV, and three time intervals before and after the eclipse, exhibit a three-peak shape indicative of a concentration of the interstellar dust grains in three discrete clouds along the line of sight. The observed profiles are fitted by the profiles of a simulated halo generated by a Monte Carlo ray-tracing code operating on a model of three discrete clouds and a spectrum of the photons emitted by the source over a period of time extending from 270 ksec before the observation began till it ended. In the model, the spectrum before the observation began is expressed as a function of the orbital phase of the pulsar and is derived as an average over 6.3 years of data accumulated by the All Sky Monitor of the *Rossi X-Ray Timing Explorer*. The distances of the two nearer dust clouds are fixed at the distances of the peaks of atomic hydrogen derived from the 21-cm spectrum in the direction of the X-ray source, namely at 1.30 and 2.56 kpc. With these constraints, a good fit is achieved with the source at a distance 4.5 kpc, the distance of the third cloud at 4.05 kpc, the total scattering optical depth of the three clouds equal to 0.159 at 3 keV, and the column density of hydrogen set to $4.6 \times 10^{22} \text{ cm}^{-2}$. With $A_V = 6.5 \pm 0.3 \text{ mag}$ for the binary companion star, QV Nor, the ratio of the scattering optical depth at 3 keV to the visual extinction is $0.0234 \pm 0.0010 \text{ mag}^{-1}$. The column density of hydrogen in the model is much greater than the column density of atomic hydrogen derived from the 21-cm spectrum, which indicates that most of the hydrogen is in molecules, probably concentrated in the three dust clouds.

Subject headings: dust, extinction—scattering—X-rays:binaries—pulsars: individual (4U 1538-52)

1. INTRODUCTION

The grain-scattered halos of X-ray sources contain clues to the nature and distribution of interstellar dust grains. The *Chandra* X-ray observatory provides the means to achieve substantial

improvements over previous observations of X-ray halos. Here we present results from a *Chandra* observation and a Monte Carlo simulation of the halo of the eclipsing X-ray binary pulsar 4U 1538-52 (hereinafter x1538), an especially interesting halo because of its comparatively high intensity, evidence in the shapes of its radial profiles for a concentration of dust in discrete clouds along the line of sight, and high variability caused by eclipses and flares.

The theory of grain-scattered halos of steady sources, first discussed by Overbeck (1965), has been developed by various authors, e.g. Slysh (1969); Hayakawa (1970); Martin (1970); Mauche & Gorenstein (1986); Smith & Dwek (1998); Draine (2003). The effects of intensity variations of a source on the variation of its halo and the possibilities this can present for measuring the distance of the source and the distribution of the scattering grains along the sight line have been discussed by Trümper & Schönfelder (1973); Alcock & Hatchett (1978); Xu, McCray & Kelley (1986); Klose (1994). Klose (1991) calculated the expected profiles of halos that would be produced by grains with various assumed size distributions. Mathis & Lee (1991) carried out an analytical study of the possibilities of using halos as diagnostics of grains. Predehl & Klose (1996) discussed the possibilities and the practical limitations of such diagnostics. Smith & Dwek (1998) showed that the Rayleigh-Gans approximation to the Mie scattering theory, commonly employed in theoretical treatments X-ray halos, yields substantial overestimates of halo intensities for photon energies less than 1 keV.

Early evidence of X-ray halos was reported by Rolf (1983) and by Catura (1983) from images recorded by the *Einstein* observatory. Mauche and collaborators (Mauche & Gorenstein 1986; Molnar & Mauche 1986; Mauche & Gorenstein 1989), employing the same observatory, found a correlation between the fractional intensity of the halo of an X-ray source and the visual extinction of its optical counterpart that was consistent with the model of solid silicate and graphite grains proposed by Mathis, Rumpl & Nordsieck (1977). Predehl & Schmitt (1995) carried out an extensive survey of X-ray halos with the *ROSAT* X-ray observatory. Witt, Smith & Dwek (2001) found evidence for a distribution in grain size extending to 2 μm and possibly more in a *ROSAT* observation of the halo of Nova Cygni 1992. Predehl et al. (2000) derived an estimate of the distance to Cyg X-3 by an analysis of its X-ray halo. Clark, Woo & Nagase (1994) employed the non-imaging *Ginga* observatory to observe x1538 and its halo. From a comparison of the counting rates before and after an eclipse of x1538 they derived an estimate of the fractional halo intensity that was substantially less than that expected on the assumption that the visual extinction of its optical companion is caused by solid silicate grains with a specific density near 3. They interpreted the result as consistent with a grain structure in the form of loose aggregates of smaller particles.

Following its discovery in the *Uhuru* galactic plane survey (Giacconi et al. 1974), x1538 was observed to pulse with a period of 529 s and to have an orbital period of 3.73 days with an eclipse lasting about 12 hours (Davison 1977; Becker et al. 1977). An accurate position determination with *SAS 3* (Apparao et al. 1978) led to identification of the highly reddened BO supergiant, QV Nor, as its companion (Crampton, Hutchings & Cowley 1978). The X-ray spectrum has a prominent iron K line (Makishima et al. 1987) and a pulse phase-dependent cyclotron resonance feature at

20 keV (Clark et al. 1990). Properties of the binary system derived from various observations are listed in Table 1.

For the present study X-ray images of x1538 and its halo were recorded before and after an eclipse immersion. Radial profiles of simulated halos, generated by a Monte Carlo ray-tracing code, were fitted to the three-peaked time-varying radial profiles of the observed halo by adjustment of the parameters of a model of the source spectrum, the dust grains, and the interstellar photoelectric absorption. The model parameters that yielded a good fit are compared with the optical extinction of QV Nor and with the column density of atomic hydrogen derived from the spectrum of 21-cm radiation in the direction of the source to derive information about the scattering efficiency of the grains and the total column density of hydrogen.

Section 2 describes the observations and data reduction. Properties of the halo are presented in section 3. The Monte Carlo simulation code is described briefly in section 4 together with the model and the fitting procedure. Section 5 is a summary and discussion of results. Section 6 lists conclusions drawn from this study.

2. OBSERVATIONS AND DATA PREPARATION

Data were obtained from the imaging spectrometer (ACIS-I) at the focal plane of the X-ray telescope of the *Chandra* observatory during a continuous 25 ksec observation (Chandra archive OBS_ID 90) beginning 2000 April 8.95 (T_0 = MJD 51642.94881) at orbital phase 0.9185, shortly before an eclipse immersion, and ending near mid-eclipse, at orbital phase 0.001. The received data for each detected photon consist of the transfer time, T , of its 3.200-s data frame, its arrival direction expressed as X(EW),Y(SN) sky coordinates in units of $0.492''$, and its energy with an uncertainty of about 0.1 keV.

Point response functions (PSFs) of the imaging system were derived from a combination of results from a 30 ksec observation of the X-ray bright quasar 3C 273 and a 12 ksec observation of the much fainter quasar PG1634+70.

We prepared arrays of the effective area per second of exposure in $3.94'' \times 3.94''$ pixels as a function of sky position, averaged over the duration of the observation and expressed in units of cm^2 per second of observation, for eighteen energies between 0.5 and 8.0 keV. In our tabulation of the received data for use in the analysis we replaced the transfer time T by $t = T - T_0$, and add the reciprocal of the effective area per second of exposure (REA) as determined according to its sky position and energy.

The arrival directions of all events in the energy range from 2 to 6 keV from the approximate beginning of total eclipse at $t = 5$ ksec to near mid-eclipse at 25 ksec are plotted relative to the direction of x1538 as dots in Fig. 1(a). The image of x1538 is in the northeast corner of the region scanned by CCD chip I3. The halo image, which persists with gradually diminishing intensity

during the eclipse, is conspicuous in a circular region spread over the four chips. Regions of the sky scanned by CCD pixels near the edges of the chips have relatively low effective areas achieved operationally by dithering the telescope orientation in a pattern centered on a fixed direction with a cycle time of 16 s. We excluded from our analysis events in these regions to avoid the large statistical fluctuations they would otherwise cause in summations of REA. We searched for other sources in the field of view by mapping all the events recorded during the interval from 1039 to 25,039 s in the energy range from 2 to 6 keV in $2'' \times 2''$ pixels. We eliminated any significant effect of other sources on the halo profiles by excluding events within $2''$ of the centers of pixels containing 5 or more events and more than $10''$ from the image center. Finally, we excluded events within $2''$ of the center line of the “transfer streak” which is the trailed image of x1538 running parallel to the southeast edge of the region scanned by chip 3 and formed during the 0.041 s shift of the CCD data to the frame store for subsequent transmission. Fig. 1(b) is a map of the events remaining after application of the exclusion criteria.

To determine the effective solid angle on the sky corresponding to a given region of the image we generated 10^4 events with random positions distributed uniformly over the region and computed the fraction of events accepted according to the exclusion criteria. The effective solid angle was evaluated as the product of that fraction times the geometrical solid angle of the region. The incident intensity of photons corresponding to a set of events recorded within a specified region of the image and interval of time was computed as the sum of the REAs of the events divided by the product of the exposure time times the solid angle. The fractional error of an intensity was estimated as the reciprocal square root of the number of events.

Data from within $2''$ of the image center recorded before the eclipse are severely degraded by pileup, i.e., multiple occurrences of events in the same pixel during the 3.200-s frame exposure. Under these circumstances the transfer streak is a useful source of data on the source flux unaffected by pileup, albeit with exposures smaller than the exposures of the frame data by the product of the fraction of the exposure time occupied by transfers (0.0128) times the fraction of the streak used. To extract the streak data, we summed the REA of events in a $4''$ -wide rectangle centered on the transfer streak and extending about half the length of the streak. Background intensity was derived from events in parallel rectangles between $3''$ and $10''$ from the center line of the streak.

During the time before the eclipse, when the incident intensity of unscattered photons from x1538 was highest, the average rate of all events in the angle range from $12''$ to $13''$ was less than $10^{-3} \text{ s}^{-1} \text{ arcsec}^{-2}$. Thus the effects of pileup on measured photon intensities at angles greater than $12''$ was negligible. We derived halo profiles from events in the angle range from $12''$ to $312''$ and preliminary estimates of the background intensities from events in the angle range from $480''$ to $600''$. Since the latter events included some halo events, background intensities were included along with the PSF normalizations among the parameters adjusted in the process of fitting the profiles of the simulated halo to the observed profiles.

3. PROPERTIES OF THE SOURCE AND HALO

3.1. Spectra and Light Curves of the Source

The pre-eclipse spectrum of the source is displayed in Fig. 2(a). It was derived from the transfer streak during seven complete pulse periods from 1037 to 4739 s. The high value in the 6.0-6.5 keV bin is due to the iron K line. The sharp decline below 4.0 keV is caused by strong circumstellar absorption that occurs as the sight line grazes the limb of QV Nor. The histogram, derived from the function

$$s_{\text{pre}}(E, t) = \left\{ I_0 E^{-1.12} + F_{\text{Fe}} \frac{\text{keV}}{\sqrt{2\pi}\sigma} \exp \left[-\frac{(E - E_{\text{Fe}})^2}{2\sigma^2} \right] \right\} \exp[-N_{\text{H}}\sigma_{\text{pe}}(E) - \tau_{\text{sca}}(E/\text{keV})^{-2}],$$

1037 s < t < 4739 s, (1)

was fitted by least squares to the data, with $F_{\text{Fe}} = 1.3 \times 10^{-3} \text{ cm}^{-2}\text{s}^{-1}$, $E_{\text{Fe}} = 6.4 \text{ keV}$, $\sigma = 0.1 \text{ keV}$, and the other parameter values listed in Table 2. The quantity $\sigma_{\text{pe}}(E)$ is the photoelectric cross section per hydrogen atom of Morrison & McCammon (1983), and N_{H} is the total column density of hydrogen along the sight line from the neutron star. The optical depth for scattering is represented by $\tau_{\text{sca}}(E/\text{keV})^{-2}$.

Fig. 2(b) displays the source spectrum during the eclipse, derived from events within $2''$ of the image center from 5 to 25 ksec when pileup caused only a small reduction in detection efficiency. During the eclipse, X-rays in the image core are fluorescent and Thomson-scattered radiation generated in distant circumstellar matter without strong circumstellar absorption. The iron K radiation is especially prominent in the eclipse spectrum.

In our analysis and simulation of the halo we restricted consideration to photons with energies in the range from 2 to 6 keV to exclude, on the high end, the iron line photons and, on the low end, low-energy photons for which the scattering cross section is less accurately represented by the Rayleigh-Gans approximation used in the simulations.

In the upper panel of Fig. 3 the incident flux of photons in the energy range from 2 to 6 keV within $2''$ of the x1538 image center is plotted as open circles against orbital phase (bottom abscissa) and time from the start of the observation (top abscissa). Solid circles show the flux derived from events in the transfer streak. In both cases integration times were set equal to the pulse period of 529 s before the eclipse and to 4952 s after the eclipse when pulsations were no longer present. The sharp drop in the streak rate near orbital phase 0.933 indicates the eclipse edge corresponding to an eclipse half-angle of $24.1^\circ \pm 0.3^\circ$. The drastically lower values of the open circles before the eclipse are caused by pileup. After the eclipse, when X-rays scattered from the circumstellar matter in the x1538/QV Nor system are still present in the source image, the core pileup is much less severe and yields values of greater statistical accuracy, though still systematically less than the streak values.

3.2. Properties of the Grain-Scattered Halo

Light curves of the background-subtracted halo in two energy ranges, 2 to 4 keV and 4 to 6 keV, are shown in the lower panel of Fig. 3. The initial decline of the halo flux at the eclipse is much less than that of the direct source due to the continuing arrival after the eclipse of photons delayed by scattering. The straight lines fitted by least squares to the data from 5 to 25 ksec show the decay of the halo flux during the eclipse.

Fig. 4 displays the spectra of the halo as average intensities in successive intervals of angle from the source direction plotted against energy. The spectra were derived from background-subtracted data recorded during the eclipse from 5 to 25 ksec. They exhibit the progressive softening with increasing angle of scattering expected from scattering theory.

Radial profiles of the halo, in two energy ranges and three time intervals before and after the eclipse, are displayed in Fig. 5. The solid circles represent values of the incident intensity of photons in thirty $10''$ intervals of angle from $12''$ to $312''$ from the source, with backgrounds and PSFs of the source subtracted. The error bars indicate the Poisson counting uncertainties of the raw data.

The profiles appear to have a three-peak shape. The outer two peaks are clearly defined by the low values of the intensities in bins 5 and 10 of panel (3) and bins 6 and 13 of panel (5). The low values in bin 1 of all three of the 2-4 keV profiles, though of low statistical significance, indicate the possible presence of a third peak. A uniform distribution of dust gives rise to a halo the profile of which, after an eclipse, develops a single broad peak whose inner bound moves toward larger angles as time from eclipse ingress increases. To explain the formation of multiple peaks, it therefore appears necessary to assume that the dust is not uniformly distributed. The problem we tackled was to find a model of the non-uniform grain distribution and the variable source spectrum that can account for the profiles of a halo produced by multiple scattering near the line of sight. We developed a Monte Carlo ray-tracing code to circumvent the difficulties of deriving halo profiles from such a model by analytical computation.

4. MONTE CARLO GENERATION OF SIMULATED HALOS

The code generates the energies, arrival directions, and arrival times of contributions to a halo from scatterings of trial photons emitted by a source with a specified variable spectrum and scattered by dust grains with a specified distribution in size and a specified distribution of the optical depth for scattering along the sight line. The code launches a specified number of trial photons from the source each second beginning far enough in the past to assure that all significant contributions to the halo during the observation are included, and ending at the termination of the observation. Each trial photon has an energy selected at random from the spectrum. It is tracked in three dimensions till it passes beyond the observer or has accumulated so great a delay in transit

as to arrive after the end of the observation.

The trajectory of a trial photon is described in a rectangular coordinate system with its origin at the source, and the Z axis along the sight line to the observer. Distance from the source along the Z axis is expressed as a fraction, z , of the total distance, D , from source to observer. The delay in the arrival time of a contribution to the halo intensity from a given scattering, relative to the arrival time of an unscattered photon, is the sum of the delays in successive path segments each of which is computed in the small angle approximation as $(z_k - z_{k-1})D\psi_k^2/2c$, where z_k is the projected position on the Z axis of the k th scattering, ψ_k is the angle that the k th segment makes with the Z axis, and c is the speed of light. The contribution to the halo intensity from each scattering is tabulated according to its energy, arrival angle, arrival time, the identification number of the dust cloud in which the scattering occurred, and the number of the scattering.

We assume the photoelectric absorption and grain scattering depend only on the Z component of position. At each scattering the size of the grain is randomly selected from a specified size distribution. We assume the probability per steradian that a photon of energy E scattered by a grain of size a will be deflected at an angle ϕ varies with size and energy according to the relation

$$\frac{dP}{d\Omega} \sim a^6 \left[\frac{F(E)}{Z} \right]^2 \Phi(u)^2, \quad (2)$$

where $\Phi(u)$ is the form factor for homogeneous spherical particles of radius a , and

$$u = \frac{4\pi Ea}{hc} \sin \frac{\phi}{2}, \quad (3)$$

where h is Planck's constant. For $E > 2$ keV and $a < 0.3 \mu\text{m}$ we can, with good accuracy, set the atomic scattering factor $F(E)/Z = 1$ (Henke 1981), and represent the form factor by the Rayleigh-Gans approximation (van de Hulst 1981),

$$\Phi(u) = 3 \frac{\sin u - u \cos u}{u^3}. \quad (4)$$

The code operates on a model that specifies

- the distance of the source;
- the time-dependent spectrum of X-ray photons coming directly from the x1538/QV Nor system before and after the observation begins;
- the distribution in size of dust grains;
- the scattering optical depth measured from the source along the line of sight as a function of z ;
- the optical depth for photoelectric absorption;

- the background intensity;
- the PSF of the imaging system.

At the conclusion of the computation the accumulated data are analyzed for the properties of the simulated halo in a manner similar to that employed with real data, but with the added feature of having available for each contribution the number of the scattering and the identification of the cloud from which it came. In addition, we sum the contributions in intervals of the launch times to check whether the specified beginning launch time is sufficiently early to capture all significant contributions to the simulated halo.

Statistical fluctuations in Monte Carlo simulations and strong cross-correlations in the effects of changes in the model parameters preclude effective use of the code in an automatic curve-fitting procedure. Instead, we sought a fit of simulated profiles to observed profiles in multiple trials with adjustments of the model parameters aimed at reducing the mean square deviation between the observed and simulated profile intensities.

Figure 14 shows a simulated halo profile that can be compared with an analytical solution computed by Mathis & Lee (1991) for a steady source of 1 keV photons scattered by $1\ \mu\text{m}$ grains distributed uniformly along the sight line with a scattering optical depth of 2. The simulated and analytical profiles of the halo components from first and second scatterings are in close agreement. Small systematic differences appear in the third and fourth scattering components which may be due to a geometrical approximation in the analytical solution, namely, the use at each scattering beyond the first of a “spherical coordinate system at the grain with a polar angle θ' measured from the point source” instead of from the previous scattering site. Figure 15 shows the evolution of this model halo that would occur following an eclipse immersion at 20 ksec and emersion at 60 ksec.

4.1. Specification of the model

In many trials, good fits of simulated profiles to the observed profiles were found with widely different sets of model parameters. Effects of a change in a given parameter can often be reversed by a compensating change in another. For example, increase in halo intensity caused by an increase in the source flux can be approximately cancelled by a decrease in the scattering optical depth that leaves the product of the two parameters unchanged. Change in the angular position of a feature in the halo of a variable source caused by a decrease in the assumed distance, d , of a scattering site can be offset by a decrease in the assumed distance D of the source that leaves the quantity $(1/d - 1/D)$ unchanged. Therefore, to obtain results that might provide useful information about the distance of the source and the properties and distribution of the dust, it was necessary to fix as many of the parameters as possible at plausible values derived from this and other observations.

Previous studies show that the spectrum of x1538 is highly variable during a single binary

orbit. To allow for this, we represent the incident spectrum at time t and orbital phase $\Pi(t)$ by

$$s_{\text{inc}}(E, t) = s_{\text{av}}(E, \Pi)[1 + f(t)] + s_{\text{pre}}(E, t) + s_{\text{ecl}}(E), \quad (5)$$

in which $s_{\text{av}}(E, \Pi)$ is the long-term average incident spectrum of photons that arrive directly from the neutron star, $[1 + f(t)]$ is a factor representing flares that may have occurred before the observation began, $s_{\text{pre}}(E, t)$ is the observed pre-eclipse spectrum of x1538 derived from the transfer streak, and $s_{\text{ecl}}(E)$ is the spectrum of photons observed during the eclipse. We assume the latter, characterizing photons produced by X-ray illumination of the circumstellar matter in the x1538/QV Nor system, is constant throughout the binary orbit.

We represent the average spectrum by

$$s_{\text{av}}(E, \Pi) = I_0 E^{-\alpha} \exp[-N_{\text{H}}(\Pi)\sigma_{\text{pe}}(E) - \tau_{\text{sca}}(E/\text{keV})^{-2}]. \quad (6)$$

The quantity $N_{\text{H}}(\Pi)$ is the column density of hydrogen between x1538 and the observer, and $\sigma_{\text{pe}}(E)$ is the photoelectric cross section per hydrogen atom. We assume $N_{\text{H}}(\Pi)$ is the sum of a constant interstellar component, N_{H}^{is} , and a variable circumstellar component,

$$N_{\text{H}}^{\text{cs}}(\Pi) = N_{\text{ecl}} \exp[-(\Pi - \Pi_{\text{ecl}})/\lambda_{\text{out}}], \quad \Pi < 0.5, \quad (7)$$

$$= N_{\text{ecl}} \exp[-(1 - \Pi - \Pi_{\text{ecl}})/\lambda_{\text{in}}], \quad \Pi > 0.5, \quad (8)$$

where Π_{ecl} is the orbital phase of total eclipse, and N_{ecl} is the column density as the sight line grazed the edge of QV Nor.

The average spectrum was derived from data in the archive of the All Sky Monitor (ASM) of the *Rossi X-Ray Timing Explorer* (RXTE). The archive provides a background-subtracted aspect-corrected count rate for a given source whenever it is in the field of view of one of three detectors during an orientation dwell in the course of its all-sky scan. We used the 16752 B-channel (nominal 3-5 keV) count rates in the range from -3.0 to 3.0 s⁻¹ of detectors 1 and 2 during the time interval from MJD 50088 to 52400 when the corresponding rates for the Crab Nebula were steady with an average of 23.08 s⁻¹. The data were folded in 50 intervals of orbital phase derived from the orbital parameters listed in Table 1. The average rates are plotted against orbital phase in Fig. 6(a). The smooth curve is the function

$$C_{3-5}^i = \int_{\Pi_{i-1}}^{\Pi_i} d\Pi \int_{3 \text{ keV}}^{5 \text{ keV}} s_{\text{av}}(E, \Pi) A(E) dE + C_0, \quad i = 1 \dots 50. \quad (9)$$

We set N_{H}^{is} and τ_{sca} to the values derived in fitting the simulated profiles to the observed profiles. The phase of total eclipse, Π_{ecl} , was set to the value indicated by the vertical line in Fig. 3. The factor $A(E)$ is the effective area of the ASM detectors normalized to yield a predicted 3-5 keV count rate for the Crab Nebula equal to the observed rate under the assumption that the Crab spectrum is $9.5(E/\text{keV})^{-2.1} \exp[-3.1 \times 10^{21} \sigma_{\text{pe}}(E)] \text{ cm}^{-2} \text{ s}^{-1} \text{ keV}^{-1}$. The function was fitted by least squares to the ASM data by adjustment of I_0 , λ_{out} , λ_{in} , and F_0 . The quantity C_0 , representing the counting

rate in eclipse, is a measure of the sum of rates due to photons scattered in the circumstellar matter of the x1538/QV Nor system, a portion of the x1538 halo, other sources in the field of view, and possible errors in the background subtraction. As such, its presence in equation (9) makes the fitted value of $I_0 E^{-\alpha}$ a good measure of the average spectrum of photons that would be incident in the absence of scattering and photoelectric absorption. We ignore the small error due to halo contamination that remains because the halo contribution to C_0 decays during the eclipse. The fixed and fitted values of the average spectrum parameters are listed in Table 3.

The observed flux of x1538 before the eclipse in the interval from 1037 to 4739 s is more than an order of magnitude larger than the value implied by the average spectrum fitted to the ASM data. The column density of the spectrum fitted to the pre-eclipse streak data, though large, is much less than that of the ASM average spectrum in the same orbital phase range. Thus it appears that there may have been, in effect, a kind of hole in the circumstellar matter that allowed an attenuated flux from x1538 to shine through. To model this portion of the pre-eclipse spectrum, which has a substantial effect on the simulated halos at small angles, we added the fitted streak spectrum previously described, $s_{\text{pre}}(E, t)$, to the model spectrum in the phase interval from 0.922 to 0.933.

We set $s_{\text{ecl}}(E) = 5.0 \times 10^{-5} \text{ cm}^{-2} \text{ s}^{-1} \text{ keV}^{-1}$ to represent the observed source spectrum during the eclipse displayed in Fig. 2(b), and which is nearly flat in the energy range from 2 to 6 keV. It made only a very small contribution to the simulated halos.

Characteristic flare phenomena of x1538 are shown in Fig. 6(b) which is a plot against orbital phase of the average counting rates of x1538 in intervals of the pulse period recorded by the Proportional Counter Array (PCA) of the RXTE in a pointed-mode observation (Clark 2000). During a flare the count rates can rise above average by a factor of five or more for several pulse periods. Photons from such a flare, scattering from dust in a discrete cloud, can produce a sharp feature in the halo profile which moves to larger angles as the time interval between the flare occurrence and the observation increases. To add a k th flare to the spectrum model we specified a constant value, f_k , of $f(\Pi)$ beginning at a certain time Π_k and lasting for an orbital phase interval of 0.01 which corresponds to a time interval of 3222 s.

With the incident spectrum before and during the observation specified, the spectrum that would be incident in the absence of interstellar photoelectric absorption and scattering is related to the incident spectrum by the equation

$$s_{\text{src}}(E, t) = s_{\text{inc}}(E, t) \exp[N_{\text{H}}^{\text{is}} \sigma(E) + \tau_{\text{sca}}(E/\text{keV})^{-2}]. \quad (10)$$

In simulations the energy of a trial photon is selected at random from this source spectrum.

The distribution in size of the grains was specified by the power law (Mathis, Rumpl & Nord-sieck 1977)

$$\frac{dn}{da} \sim a^{-3.5}, \quad a_{\text{min}} < a < a_{\text{max}}. \quad (11)$$

We call $\tau(z)(E/1 \text{ keV})^{-2}$ the optical depth from the source to z for scattering photons of energy E , and note that $\tau(1) = \tau_{\text{sca}}$. For a clue to the distribution of the dust grains along the sight line we examined the spectrum of 21-cm radiation in the direction of x1538 ($l^{\text{II}}=327^\circ.4$, $b^{\text{II}}=2^\circ.1$), kindly provided by N. McClure-Griffiths from the Southern Galactic Plane Survey (McClure-Griffiths 2001) and displayed in Fig. 7(a). The sight line is sufficiently inclined with respect to the galactic plane so that we can safely assume most of the hydrogen along it lies between Earth and the tangent point at 6.7 kpc. Assuming $R_0 = 8.0$ kpc and $R\Omega(R) = 220 \text{ km s}^{-1}$, we converted the Doppler velocities to radial distance to obtain the brightness temperature as a function of distance, d , as plotted in Fig. 7(b).

We explored the viability of a model with dust density simply proportional to the brightness temperature, i.e., $\tau(d/D) \propto T_b(d)$, and the source spectrum described above without flares. Fig. 8 illustrates the gross failure of such a model to yield a simulated halo with a profile that conforms to the peaks and valleys of the observed profiles.

A halo due to scattering from a uniform distribution of dust decays slowly outward from the center, giving rise to a profile with a peak that moves to larger angles as time from eclipse ingress increases. If the dust is concentrated in a narrow cloud, the hollowing out occurs more rapidly. The rate at which the peak moves toward larger angles depends on the location of the cloud and the distance of the source. With this in mind, and with the intent to produce multi-peaked profiles with a model of dust concentrated in several narrow clouds, we call $\tau_k(E/1 \text{ keV})^{-2}$ the scattering optical depth of the k th cloud at distance d_k for photons of energy E with τ_k distributed uniformly from $z_k = 1. - d_k/D$ to $z_k + 0.01$. With all the grains located in such clouds, $\tau_{\text{sca}} = \Sigma \tau_k$.

We placed two clouds at the distances of the two prominent peaks of atomic hydrogen density at $d_1 = 1.30$ kpc and $d_2 = 2.56$ kpc, and explored how well the resulting two peaks in the profile intensity could be made to conform to the outer two peaks of the observed profiles by adjustment of the source distance and the cloud thicknesses. With $d_1 = 1.30$ kpc and $d_2 = 2.56$ kpc, and with τ_1 and τ_2 adjustable, we generated halos for source distances of 4.0, 4.5, 5.0, and 6.0 kpc, all within the wide range of uncertainties of published estimates based on photometric measurements of QV Nor. As in the previous example, we assumed the source spectrum was as described above without flares. The results, displayed in Fig. 9, show that the peaks shift, as expected, to larger angles as the source distance is increased. For distances of 5 and 6 kpc the simulated profiles are poor matches to the observed profiles. The fit for 4.5 appears slightly better than for 4.0 kpc. Though 4.5 kpc is near the lower limit of photometrically plausible distances, we adopted it for the model, with the expectation that the poor fit at angles below $60''$ could be repaired by placing a third cloud closer to the source.

4.2. Fitting Simulated Profiles to the Observed Profiles

The six profiles displayed as solid circles with error bars in Fig. 11 were the targets of the fitting process. They were compiled from the same data as were the six profiles in Fig. 5, but without subtraction of the background and the point spread functions. To achieve a fit, we added a third cloud to the model, and reduced the rms deviation between the simulated and observed profiles as much as seemed possible by adjusting a_{\max} , τ_1 , τ_2 , d_3 , τ_3 , and N_{H}^{is} , together with the background levels, and the normalization factors of the point spread functions. As expected, we could increase the intensity of a given profile peak by increasing the scattering optical depth of the corresponding cloud, but with correlated effects on the other peaks due to shifts in the relative frequencies of scattering in the other two clouds. We could increase the ratio between the intensities in the 4-6 and 2-4 keV profiles by increasing N_{H}^{is} .

We then sought values of the occurrence times and magnitudes of flares that could cause single-bin deviations to mimic those that seemed to be present, for example, in bin 18 in panel 3 and bin 15 in panel 5. The choice of occurrence times was guided by the equation

$$\theta = \left[2c(t - t') \left(\frac{1}{d} - \frac{1}{D} \right) \right]^{1/2}, \quad (12)$$

which expresses the arrival angle of a photon emitted at time $t' - D/c$ from the source which arrives at time t after scattering from a grain at distance d from the observer. We note that with three clouds the effects of one flare appear around three separate angles. Thus adding a flare to the model had subtle effects that reduced the overall rms deviation of the fit, but are not all evident to the eye.

Table 4 lists the fixed and fitted parameters of the final model, and Fig. 10 displays some of the control data in graphical form. The intensities of the resulting simulated profiles are plotted as the open circles in Fig. 11. The curves indicate the sums of the backgrounds and point spread functions that were added to the simulated profiles. Plotted below the profiles are the deviations of the simulated data from the observed data divided by the one-sigma statistical errors of the observed data. The quality of the fit for each profile is indicated in the plot by the rms deviation. The rms deviation of the total fit is 0.88. The statistical uncertainties of the simulated data were negligibly small by virtue of the large number (10^4) of trial photons launched per second, which yielded $\sim 3.4 \times 10^7$ contributions to the simulated data.

The separate contributions to the simulated profiles by scatterings from the three dust clouds are plotted in Fig. 12.

Another test of the simulation is provided by the comparison between the spectra of the observed and simulated halos displayed in Fig. 13. Both the observed and simulated spectra were compiled from data in the angle range from $30''$ to $200''$ and the time range from 5037 to 25037 s.

Although a good fit has been obtained with the listed parameters, a substantial uncertainty must be attached to each of them. A major source of that uncertainty is the use of the ASM

average spectrum for lack of specific information about the spectrum during the period of ~ 2 days before the observation began. Another source of uncertainty are the cross correlations among the effects of variations of the various model parameters which result in a very flat chi-square function of the overall fit. We found that a good fit can be achieved with the source distance fixed at 6 kpc, provided the distances of the two nearer dust clouds are changed to 1.42 and 3.20 kpc, well away from the distances of the atomic hydrogen concentrations derived from the 21-cm spectrum. Fixing the distances of the two principal dust clouds did place a significant constraint on the choice of the adjusted parameters. Nevertheless, lacking an objective procedure for evaluating the uncertainties in the fitted parameters that arise from these ambiguities, we have listed the values that yielded the fit without errors.

5. SUMMARY OF RESULTS AND DISCUSSION

The profiles of the grain-scattered halo of x1538, recorded before and after an eclipse, have been fitted by the profiles of a simulated halo generated by a Monte Carlo ray-tracing program operating on a model of the dust grains and the source spectrum. In the model the dust is concentrated in three discrete clouds of which the two responsible for most of the scattering are fixed at the distances of two peaks in the density of atomic hydrogen derived from the 21-cm spectrum, namely 1.30 and 2.56 kpc. The source spectrum before the observation began was assumed to be an average derived from several years of observations by the All Sky Monitor on the it RXTE X-ray observatory. The essential fitted parameters of the model were the distance of x1538, the distance of the third cloud, the scattering optical depths of all three clouds, and the column density of hydrogen. Three flares were added to the model spectrum before the observation began with occurrence times and magnitudes adjusted to mimic sharp features in the observed profiles.

The model parameters of general significance are the source distance, the total scattering optical depth, the interstellar photoelectric absorption, and the upper limit on the grain size.

Locating the two principal dust clouds at the peaks in the density of atomic hydrogen forced a choice of the source distance in the fitting model that is substantially less than the estimates of 6.0 kpc and 6.4 kpc derived from photometry of QV Nor, respectively, by Ilovaisky, Chevalier & Motch (1979) and Reynolds, Bell & Hilditch (1992). The adopted value of 4.5 kpc is in the low end of the uncertainty range of the estimate obtained from photometry by Crampton, Hutchings & Cowley (1978).

The ratio

$$R_{\text{xv}}(E) = \tau_{\text{sca}}(E/\text{keV})^{-2}/A_V \quad (13)$$

is a measure of the scattering efficiency of the grains for photons of energy E . In this ratio, A_V is the visual extinction of the optical companion, QV Nor. In the fitted model, $\tau_{\text{sca}}(E/\text{keV})^{-2} = 0.159$ for $E = 9$ keV. Assuming $A_V = 6.8 \pm 0.3$ mag for the visual extinction of QV Nor, we find $R_{\text{xv}}(3 \text{ keV}) = 0.0234 \pm 0.0010 \text{ mag}^{-1}$, where the stated error includes only the uncertainty range of

the published values of the visual extinction. This result contradicts the much lower value derived from the *Ginga* observation of x1538 previously cited (Clark, Woo & Nagase 1994). However, it is somewhat lower than the theoretical value of 0.0272 read from the plot computed by Draine (2003) for solid spherical carbonaceous and silicate grains, and is consistent with the idea that interstellar dust grains are not compact.

The value of N_{H} required to match the ratio of the 2-4 keV halo intensities to the 4-6 keV intensities, like the values obtained from other observations of x1538, is much larger than the integrated column density of atomic hydrogen derived from the 21-cm Doppler spectrum in the direction of x1538. The latter, computed according to the equation (Burke & Graham-Smith 2002)

$$N_{\text{H}} = 1.8 \times 10^{18} \int T_{\text{b}} dv \text{ cm}^{-2}, \quad (14)$$

is plotted against radial distance in Fig. 7(c). If the photoelectric cross section per hydrogen atom we have used is accurate, then most of the hydrogen along the sight line to x1538 must be in molecules, presumably in the three dust clouds.

6. CONCLUSIONS

From this study we conclude:

- 1) Monte Carlo simulation of a grain-scattered X-ray halo can provide an effective means for extracting information about the distance of the source and the properties and distribution of interstellar dust grains in circumstances involving discrete dust clouds, source variability, and multiple scattering.
- 2) To reduce uncertainty in such a simulation it is essential to have an accurate record of the source spectrum for an extended period before the halo observation begins.
- 3) The halo of x1538 is an especially interesting object because of its relatively high surface brightness, complex structure, and high variability due to eclipses and flares.
- 4) The time-varying three-peaked halo profiles of x1538 before and after an eclipse can be fitted by simulated halo profiles generated by a Monte Carlo ray-tracing code operating on a model with the source at 4.5 kpc, three discrete dust clouds of which two are at the distances of the two greatest concentrations of atomic hydrogen derived from the 21-cm spectrum, and a third cloud closer to the source.
- 5) The total scattering optical depth of the three dust clouds in the model is 0.159 for $E = 3$ keV. The ratio of this quantity to the visual extinction of the optical companion, QV Nor, is $0.0234 \pm 0.0010 \text{ mag}^{-1}$, somewhat less than the theoretical value of 0.0272 derived for solid spherical carbonaceous and silicate grains by Draine (2003).

I thank Mark Bautz, John Arabadjis and the Chandra support staff for help in use of the *Chandra* data system, and Ronald Remillard, Allan Levine, and Edward Morgen for advice in the interpretation of the RXTE data. I thank Naomi McClure-Griffiths for providing the 21-cm spectrum in the direction of x1538.

REFERENCES

- Alcock, C. & Hatchett, S. 1978, *ApJ*, 222, 456
- Apparao, K. M. V., Bradt, H. V., Dower, R. G., Doxsey, R. E., Jernigan, J. G., & Li, F. 1978, *Nature*, 271, 225
- Becker, R. H., Swank, J. H., Boldt, E. A., Holt, S. S., Serlemitsos, P. J., Pravdo, S. H. & Saba, J. R. 1977, *Ap. J. (Letters)*, 216, 11
- Burke, B. F. & Graham-Smith, F. 2002, *An Introduction to Radio Astronomy* (Cambridge: Cambridge University Press)
- Catura, R. C. 1983, *ApJ*, 275, 645
- Clark, G. W., Woo, J. W., Nagase, F., Makishima, K., & Sakao, T. 1990, *ApJ*, 353, 274
- Clark, G. W., Woo, J., & Nagase, F. 1994, *ApJ*, 422, 336
- Clark, G. W. 2000, *ApJ*, 542, L131
- Crampton, D., Hutchings, J. B., & Cowley, A. P. 1978, *ApJ*, 225, L63
- Davison, P. J. N. 1977, *MNRAS*, 179, 35p
- Draine, B. T. 2003, *ApJ*, 598, 1026
- Giacconi, R., Murray, S., Gursky, H., Kellogg, E., Schreier, E., Matilsky, T., Koch, D., & Tananbaum, H. 1974, *ApJS*, 178, 281
- Hayakawa, S. 1970, *Progr. Theor. Phys.*, 43,1224
- Henke, B. L. 1981, in *Low Energy X-Ray Diagnostics*, ed. D. T. Attwood & B. l. Henke (New York: AIP),146
- Ilovaisky, S. A., Chevalier, C., & Motch, C. 1979, *A&A*, 71, L17
- Klose, S. 1991, *A&A*, 248, 624
- Klose, S. 1994, *A&A*, 289, L1
- Makishima, K., Koyama, K., Hayakawa, S., & Nagase, F. 1987, *ApJ*, 314, 619
- Martin, P. G. 1970, *MNRAS*, 149, 221
- Mathis, J. S., Rumpl, W., & Nordsieck, K. H. 1977, *ApJ*, 217,425
- Mathis, J. S., & Lee, C. -W. 1991, *ApJ*, 376, 490
- Mauche, C. W., & Gorenstein, P. 1986, *ApJ*, 302, 371

- Mauche, C. W., & Gorenstein, P. 1989, *ApJ*, 336,843
- McClure-Griffiths, N. 2001, private communication
- Molnar, L. A., & Mauche, C. W. 1986. *ApJ*, 310, 343
- Morrison, R., & McCammon, D. 1983,*ApJ*, 270, 119
- Overbeck, J. 1965, *ApJ*, 141, 864
- Pakull, M., van Amerongen, S., Bakker, R. & van Paradijs, J. 1983, *A&A*, 122, 79
- Predehl, P., & Klose, S. 1996, *A&A*, 306, 283
- Predehl, P., & Schmitt, J. H. M. M. 1995, *A&A*, 293, 889
- Predehl, P., Burwitz, V., Paerels, F., & Trümper, J. 2000, *A&A*, 357, L25
- Reynolds, A. P., Bell, S. A., & Hilditch, R. W. 1992, *MNRAS*, 256, 631
- Robba, N. R., Burderi, L., Di Salvo, T., Iaria, R., & Cusumano, G. 2001, *ApJ*562, 950
- Rolf, D. P. 1983, *Nature*, 302,46
- Slysh, V. I. 1969, *Nature*, 224, 159
- Smith, R., & Dwek, E. 1998, *ApJ*, 503, 831
- Smith, R. K., Edgar, R. J., & Shafer, R. A. 2002, *ApJ*, 581, 562
- Trümper, J., & Schönfelder, V. 1983, *A&A*, 35, 445
- van de Hulst, H. C. 1981, *Light Scattering by Small Particles* (New York: Dover)
- Witt, A. N., Smith, R. K., & Dwek, E. 2001, *ApJ*, 550, L201
- Xu, Y., McCray, R., & Kelley, R. 1986, *Nature*, 319, 652

Table 1. Parameters of the 4U 1538-52/QV Nor Binary System

4U 1538-52 (ref. 5)	QV Nor	ref.
Epoch=MJD 50449.93400	D=5.5 ± 1.5 kpc	1
$a_x \sin i = 56.6 \pm 0.7$ lt-s	=6.0 ± 0.5 kpc	2
$T_{\pi/2}$ =MJD 50450.206 ± 0.014	=6.4 ± 1.0 kpc	4
$P_{\text{pulse}} = 528.809 \pm 0.008$ s	$A_V = 6.5$ mag	1
$\dot{\nu}_{\text{pulse}} = (-0.4 \pm 2.3) \times 10^{-13}$ Hz s ⁻¹	=7.1 mag	2
$e = 0.174 \pm 0.015$	=6.9 mag	3
$\omega = 64^\circ \pm 9^\circ$		
$a_0^{\text{a}} = 47221.488 \pm 0.015$ d		
$a_1^{\text{a}} = 3.728366 \pm 0.000032$ d		
$a_2^{\text{a}} = (-5.5 \pm 4.0) \times 10^{-8}$ d		
$P_{\text{orb}} = a_1 + 2a_2N$		
$\dot{P}_{\text{orb}}/P_{\text{orb}} = (-2.9 \pm 2.1) \times 10^{-6}$ yr ⁻¹		

$$^{\text{a}}T_{\pi/2}(N) = a_0 + a_1N + a_2N^2$$

References. — (1)Crampton, Hutchings & Cowley (1978);
(2) Ilovaisky, Chevalier & Motch (1979); (3) Pakull et al. (1983);
(4)Reynolds, Bell & Hilditch (1992); (5) Clark (2000)

Table 2. Spectrum parameters of x1538 in the energy range less than 6 keV from various satellite observations.

satellite	$I_0(\times 10^{-2})$ $\text{cm}^{-2} \text{ s}^{-1} \text{ keV}^{-1}$	α	$N_{\text{H}}(\times 10^{22})$ cm^{-2}	τ_{sca}	orbital phase	ref.
<i>Tenma</i>	3.7 ± 0.3	1.12 ± 0.04	3.7 ± 0.4	0.0	high state	1
<i>Ginga</i>	4.87 ± 0.14	1.19 ± 0.02	2.0	0.0	0.28-0.45	2
<i>SAX</i>	6.6 ± 0.4	1.12	1.80 ± 0.1	0.0	0.50-0.65	3
	4.3 ± 0.2	0.97	1.40 ± 0.1	0.0	0.65-0.75	3
<i>Chandra</i>	3.4 ± 0.5	1.12	16.5 ± 0.5	1.42	0.921-0.933	4

References. — (1) Makishima et al. (1987); (2) Clark, Woo & Nagase (1994); (3) Robba et al. (2001); (4) present data.

Note. — The spectra have the form
 $I(E) = I_0 \exp[-N_{\text{H}}\sigma(E) - \tau_{\text{sca}}(E/\text{keV})^{-2}](E/\text{keV})^{-\alpha}$.

Table 3. Parameters of the function fitted to the folded light curve of x1538 compiled from the RXTE-ASM data archive.

FIXED	FITTED
$\Pi_{\text{ecl}} = 0.0675$	$I_0 = 4.03 \times 10^{-2} \text{ cm}^{-2} \text{ s}^{-1} \text{ keV}^{-1}$
$N_{\text{H}}^{\text{ecl}} = 3.0 \times 10^{25} \text{ cm}^{-2}$	$\lambda_{\text{out}} = 0.263$
$N_{\text{H}}^{\text{is}} = 4.6 \times 10^{22} \text{ cm}^{-2}$	$\lambda_{\text{in}} = 0.258$
$\tau_{\text{scat}} = 1.431$	$C_0 = 3.94 \times 10^{-2} \text{ s}^{-1}$
$\alpha = 1.12$	

Table 4. Fixed and fitted parameters of the halo simulation model.

FIXED	FITTED
$I_{\text{av}} = 4.03 \times 10^{-2} \text{ cm}^{-2} \text{ s}^{-1} \text{ keV}^{-1}$	$D = 4.5 \text{ kpc}$
$a_{\text{min}} = 0.0003 \text{ } \mu\text{m}$	$N_{\text{H}}^{\text{is}} = 4.6 \times 10^{22} \text{ cm}^{-2}$
$\alpha = 1.12$	$a_{\text{max}} = 0.27 \text{ } \mu\text{m}$
$\lambda_{\text{out}} = 0.263$	$\tau_1 = 0.962$
$\lambda_{\text{in}} = 0.258$	$\tau_2 = 0.321$
$\Pi_{\text{ecl}} = 0.0675$	$d_3 = 4.05 \text{ kpc}$
$N_{\text{H}}^{\text{ecl}} = 3.00 \times 10^{25} \text{ cm}^{-2}$	$\tau_3 = 0.148$
$I_{\text{pre}} = 3.49 \times 10^{-2} \text{ cm}^{-2} \text{ s}^{-1} \text{ keV}^{-1}$	$\tau_{\text{sca}} = 1.431$
$N_{\text{H}}^{\text{pre}} = 16.5 \times 10^{22} \text{ cm}^{-2}$	$t_1 = -9.12 \text{ ksec}$
$I_{\text{ecl}} = 5.00 \times 10^{-5} \text{ cm}^{-2} \text{ s}^{-1} \text{ keV}^{-1}$	$f_1 = 6.0$
$d_1 = 1.30 \text{ kpc}$	$t_2 = -67.18 \text{ ksec}$
$d_2 = 2.56 \text{ kpc}$	$f_2 = 1.5$
	$t_3 = -115.51 \text{ ksec}$
	$f_3 = 1.7$

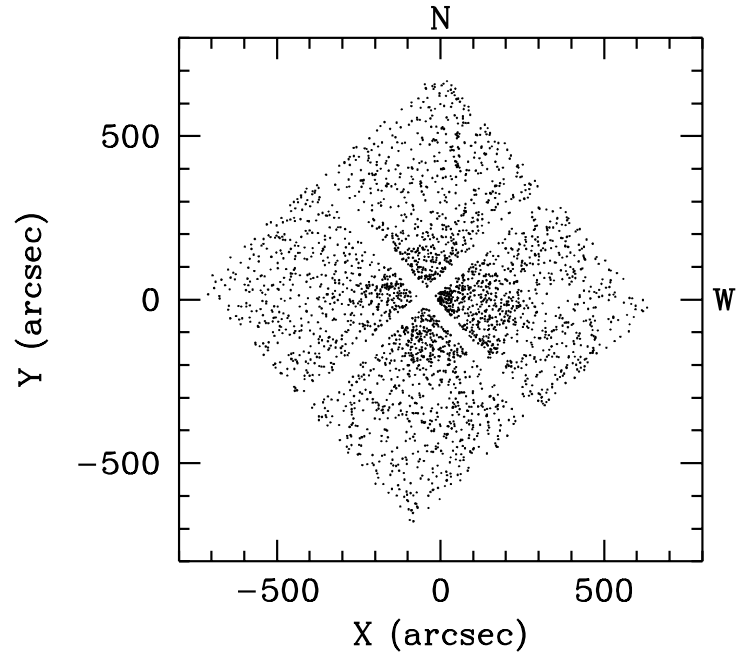


Fig. 1.— Map of events from the observation of x1538 recorded after application of rejection criteria.

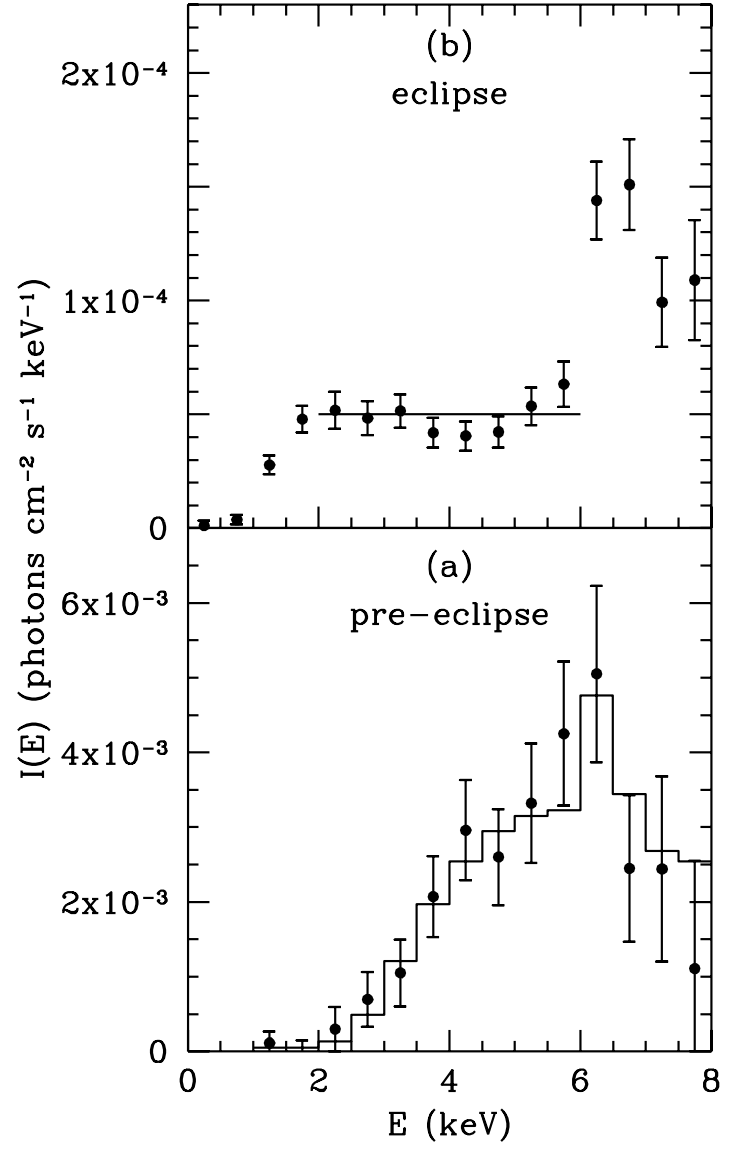


Fig. 2.— (a) Pre-eclipse spectrum of x1538 derived from the transfer streak. (b) Post-eclipse spectrum derived from events within $2''$ of the image center.

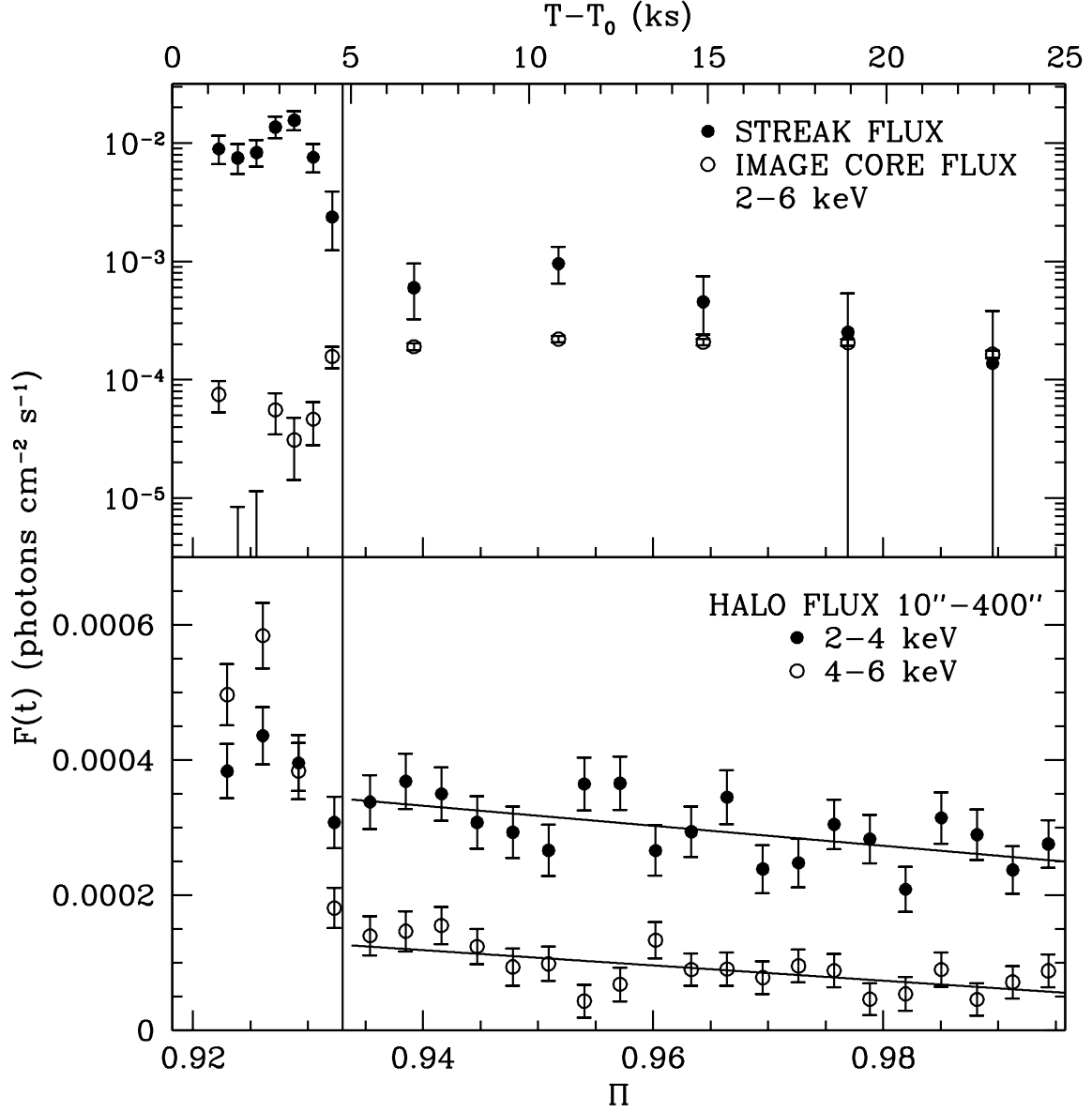


Fig. 3.— Incident fluxes of photons causing accepted events plotted against time from the start of the observation and orbital phase. In the upper panel the values shown as solid circles are derived from events in the transfer streak; the open circles show values derived from events within 2'' of the image center and depressed by pileup in the CCD chip of the ACIS. The lower panel shows the background-subtracted halo flux in two energy ranges. Straight lines were fitted by least squares to the halo intensities after 5 ksec to show the decay of the halo during the eclipse.

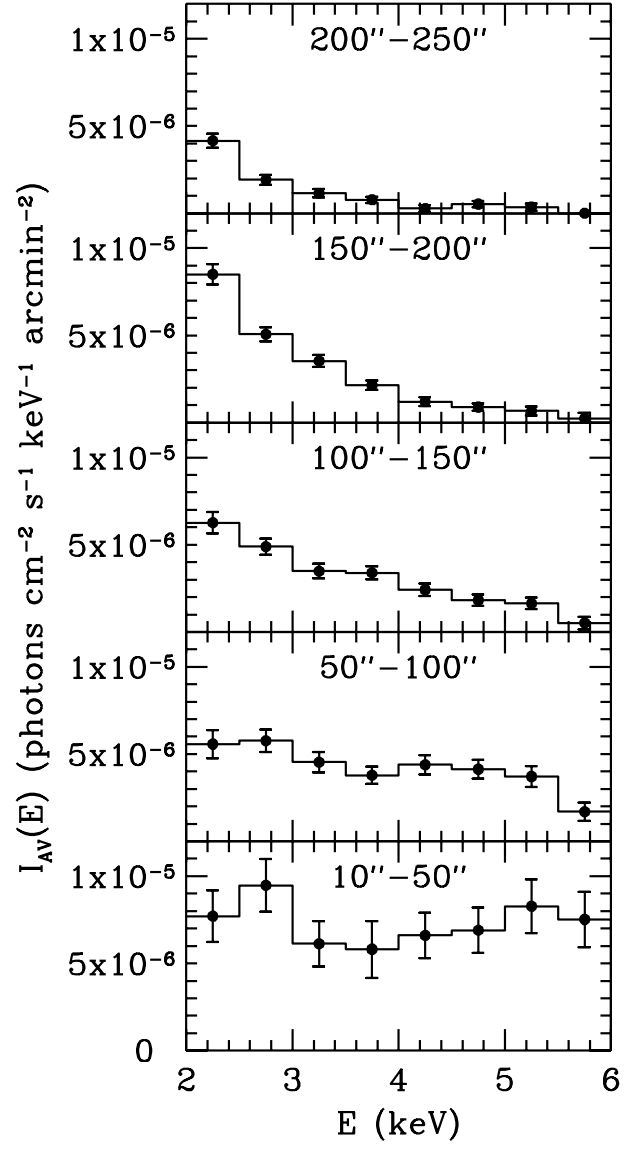


Fig. 4.— Spectra of the grain-scattered halo in five intervals of angle from the image center.

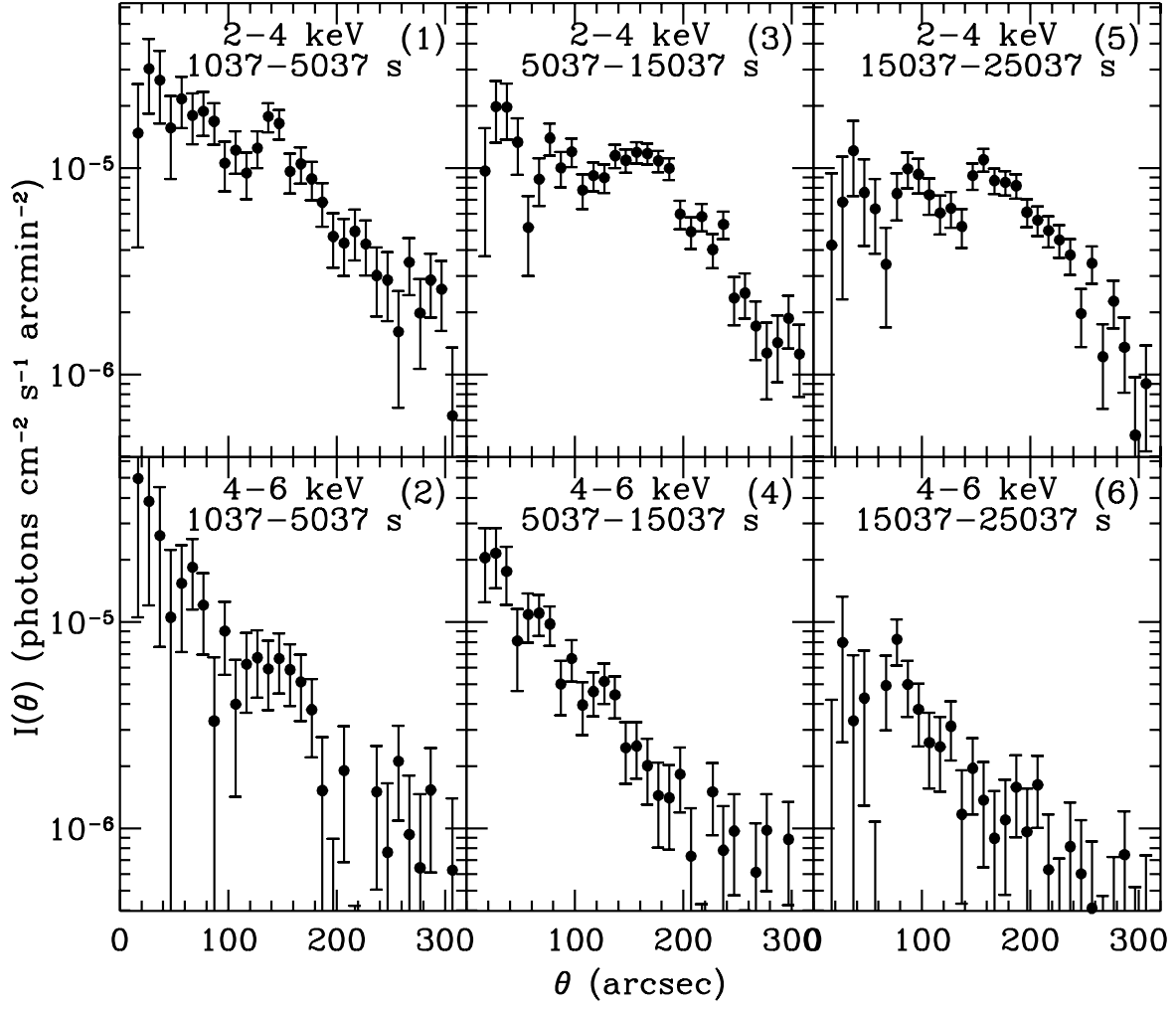


Fig. 5.— Halo profiles in two energy ranges and three time intervals. The surface brightness is plotted as intensity against angle from the image center after subtraction of the PSF of the source image and the background.

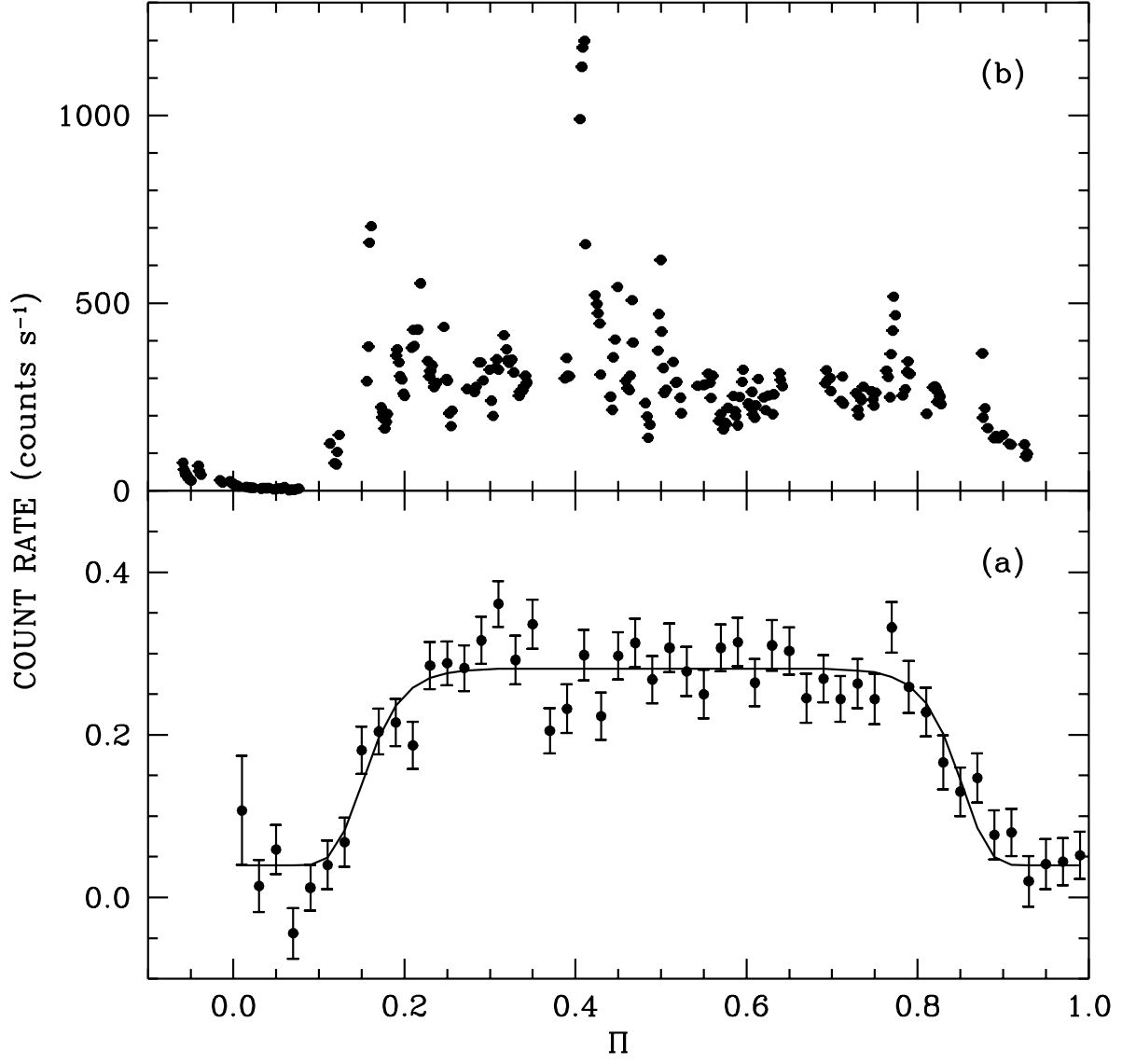


Fig. 6.— (a) RXTE-ASM count rates of x1538 in fifty equal intervals of orbital phase averaged over 6.91 yr. (b) Average background-subtracted RXTE-PCA count rates of x1538 in intervals of 529 s plotted against orbital phase as recorded in an observation during one nearly complete binary orbit.

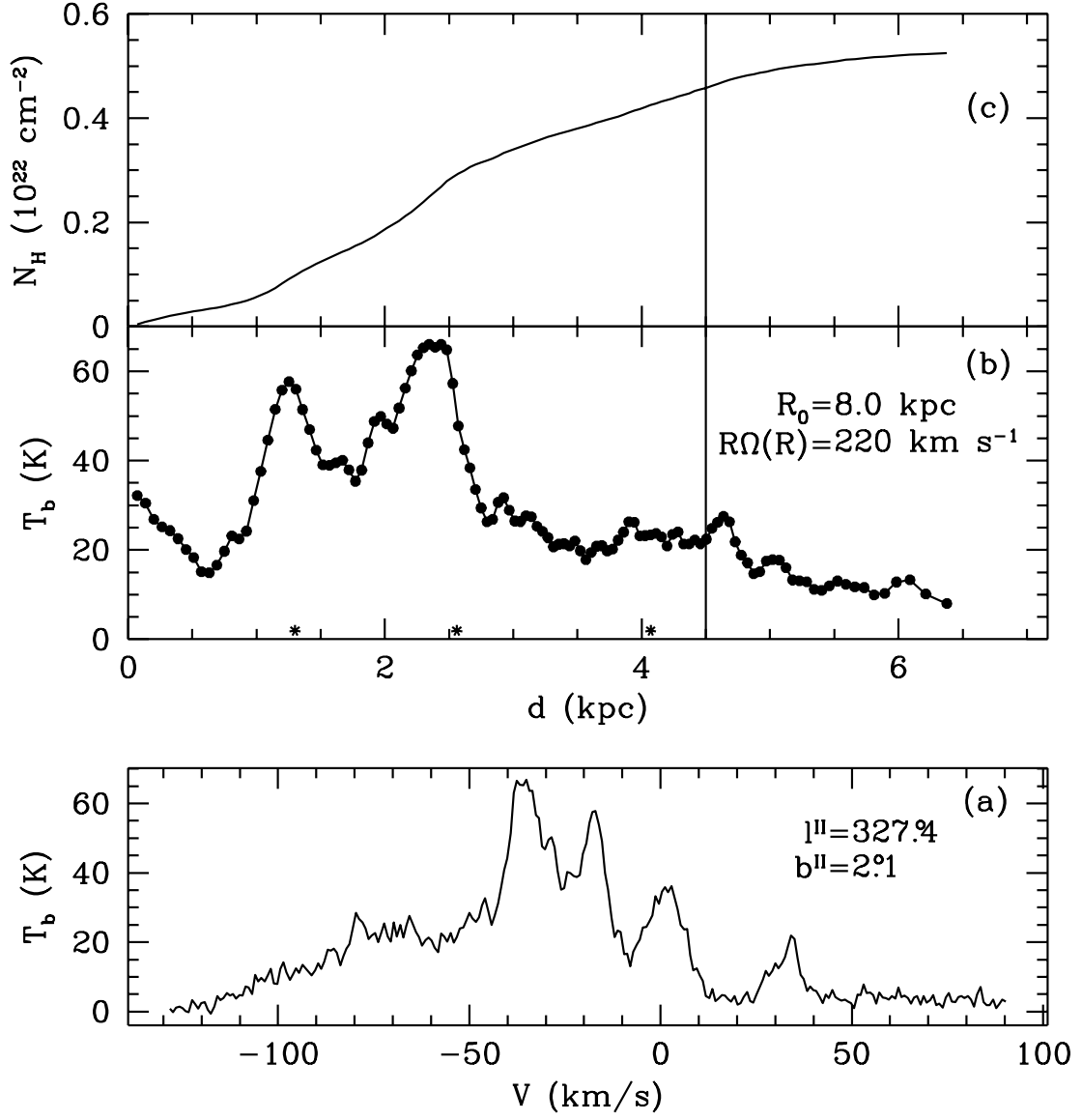


Fig. 7.— (a) Brightness temperature of 21-cm radiation plotted against radial velocity in the direction of x1538. (b) Brightness temperature plotted against radial distance toward x1538. The asterisks mark the distances of the dust clouds and the vertical line the distance of the source in the simulation model. (c) Column density of atomic hydrogen plotted against distance toward x1538.

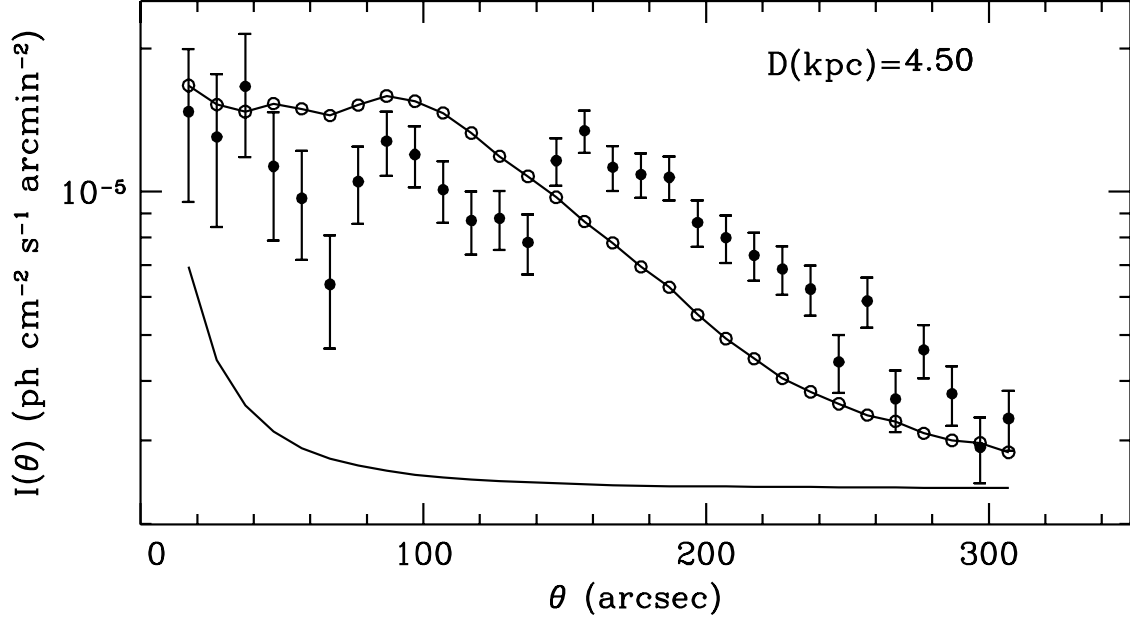


Fig. 8.— Comparison of the observed halo profile (solid circles) in the interval from 15037 to 250037 s and energy range from 2 to 4 keV with the profile (open circles) of a halo generated from a model of dust distributed with $\tau(d/D) \propto T_b(d)$. The observed profile intensities include background and PSF intensities. The lower curve indicates the contribution of the background and PSF to the simulated profile.

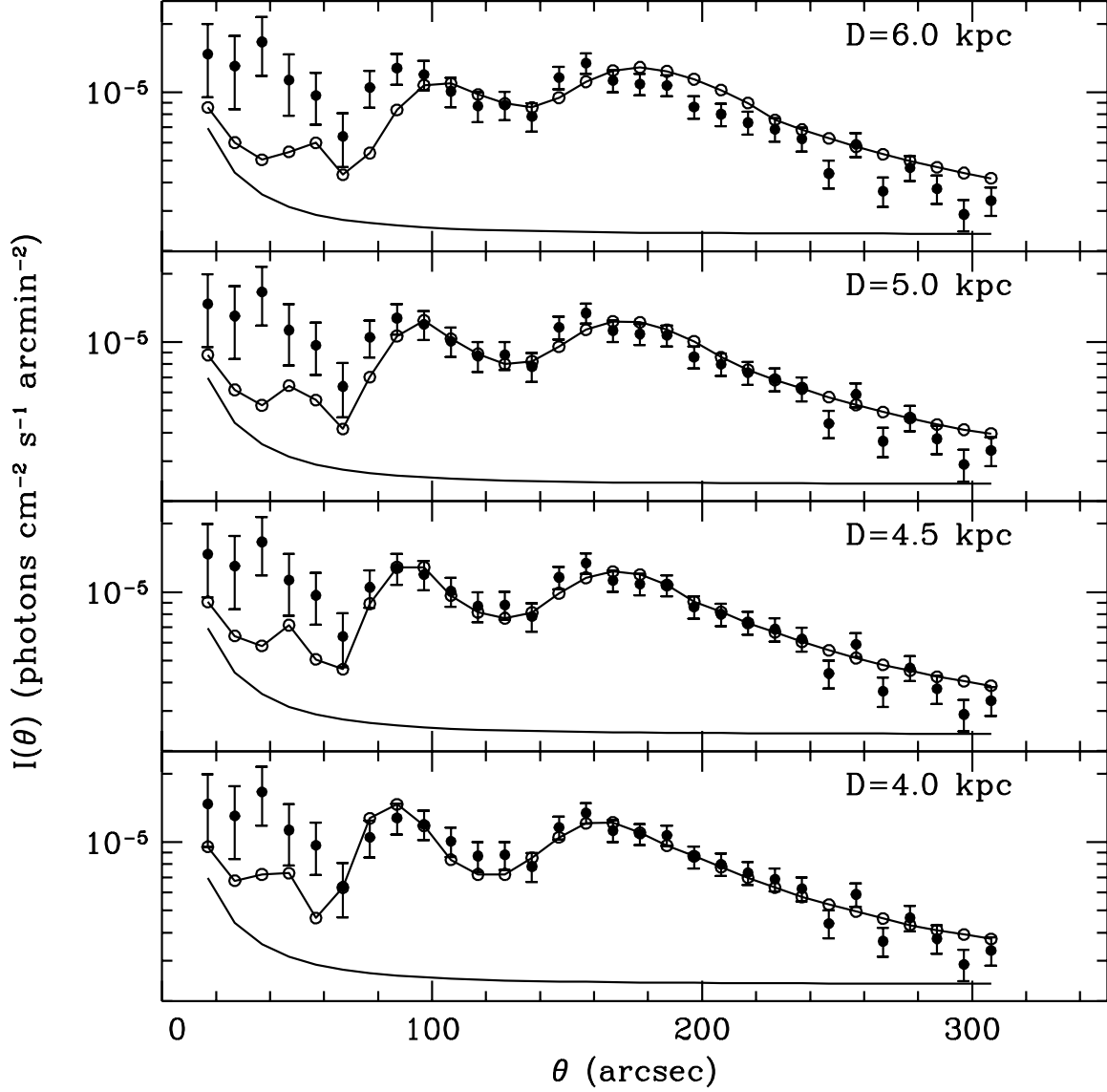


Fig. 9.— Comparison of the observed halo profile in the interval from 15037 to 25037 s and energy range from 2 to 4 keV with fitted simulated halo profiles for various assumed source distances. In the models two narrow dust clouds with adjustable scattering optical depths were placed at the distances of the two main peaks of brightness temperature in the radio spectrum of 21-cm radiation in the direction of x1538. The poor fits for angles less than $60''$ indicate the need for a third cloud closer to the source.

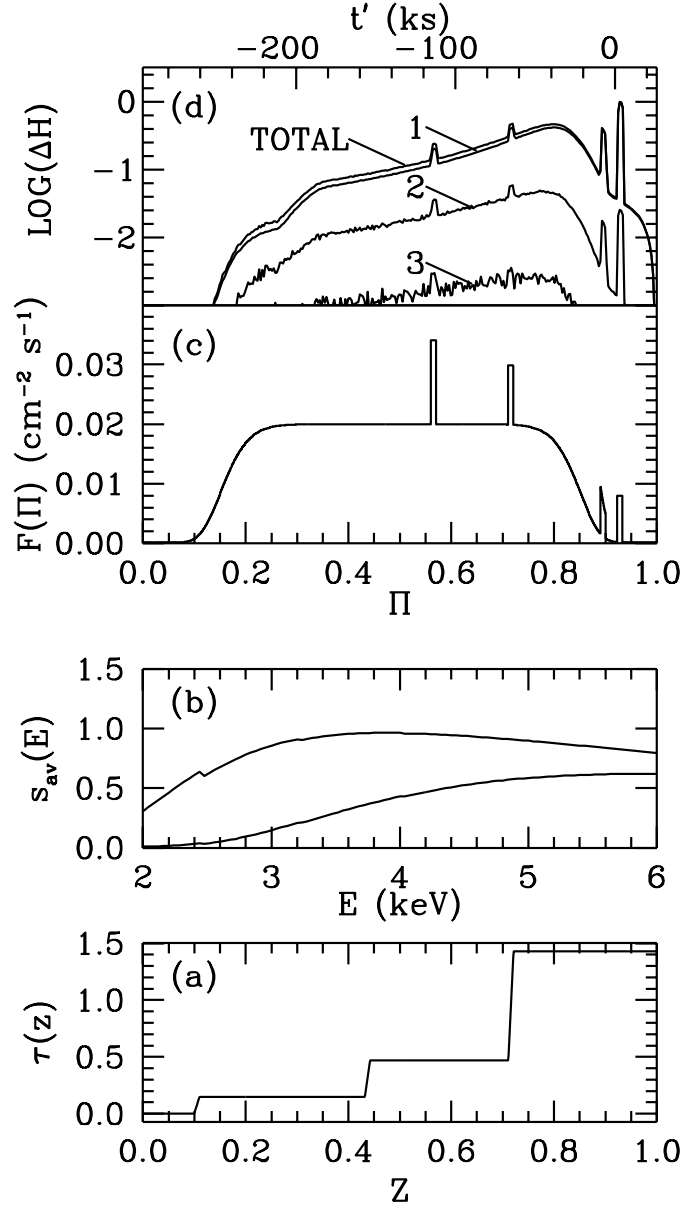


Fig. 10.— Simulation model data. (a) Scattering optical depth parameter plotted against fractional distance from the source; (b) Incident average source spectra at two phases of the binary orbit: top curve at orbital phase 0.5, bottom curve at orbital phase 0.92 when circumsource photoelectric absorption is strong; (c) Model incident source flux of 2-6 keV photons plotted against reduced emission time and orbital phase. The apparent flare after $t' = 0$ represents the observed pre-eclipse spectrum; (d) Relative contributions to the halo flux by photons scattered once, twice, thrice, and their sum plotted against the reduced emission time.

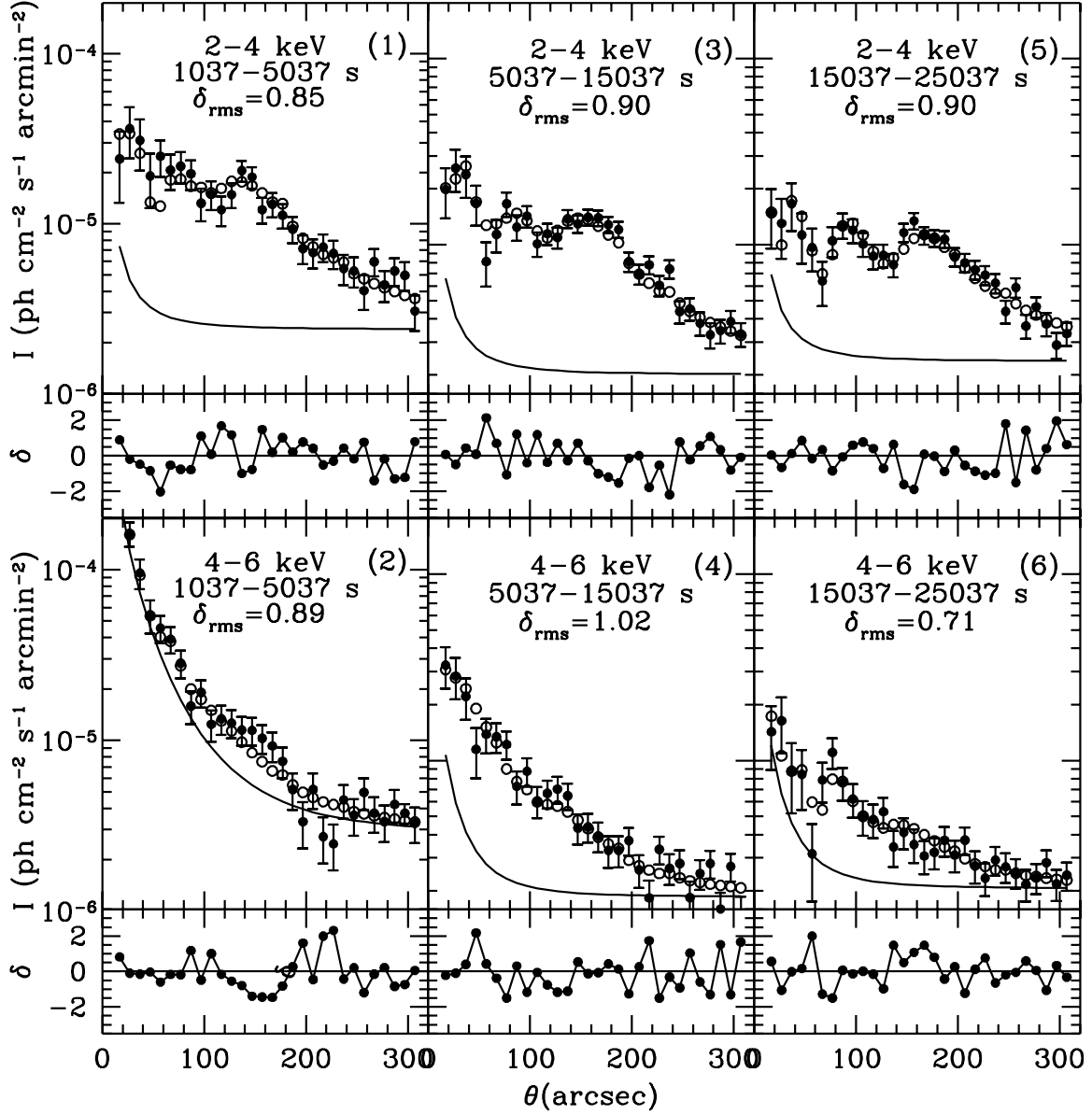


Fig. 11.— Observed halo profiles without subtraction of background and PSFs of the central image (solid circles) and fitted simulated halo profiles (open circles). The curves are the sums of the fitted backgrounds and PSFs that were added to the simulated halo data. The rms deviation of all six fits is 0.88.

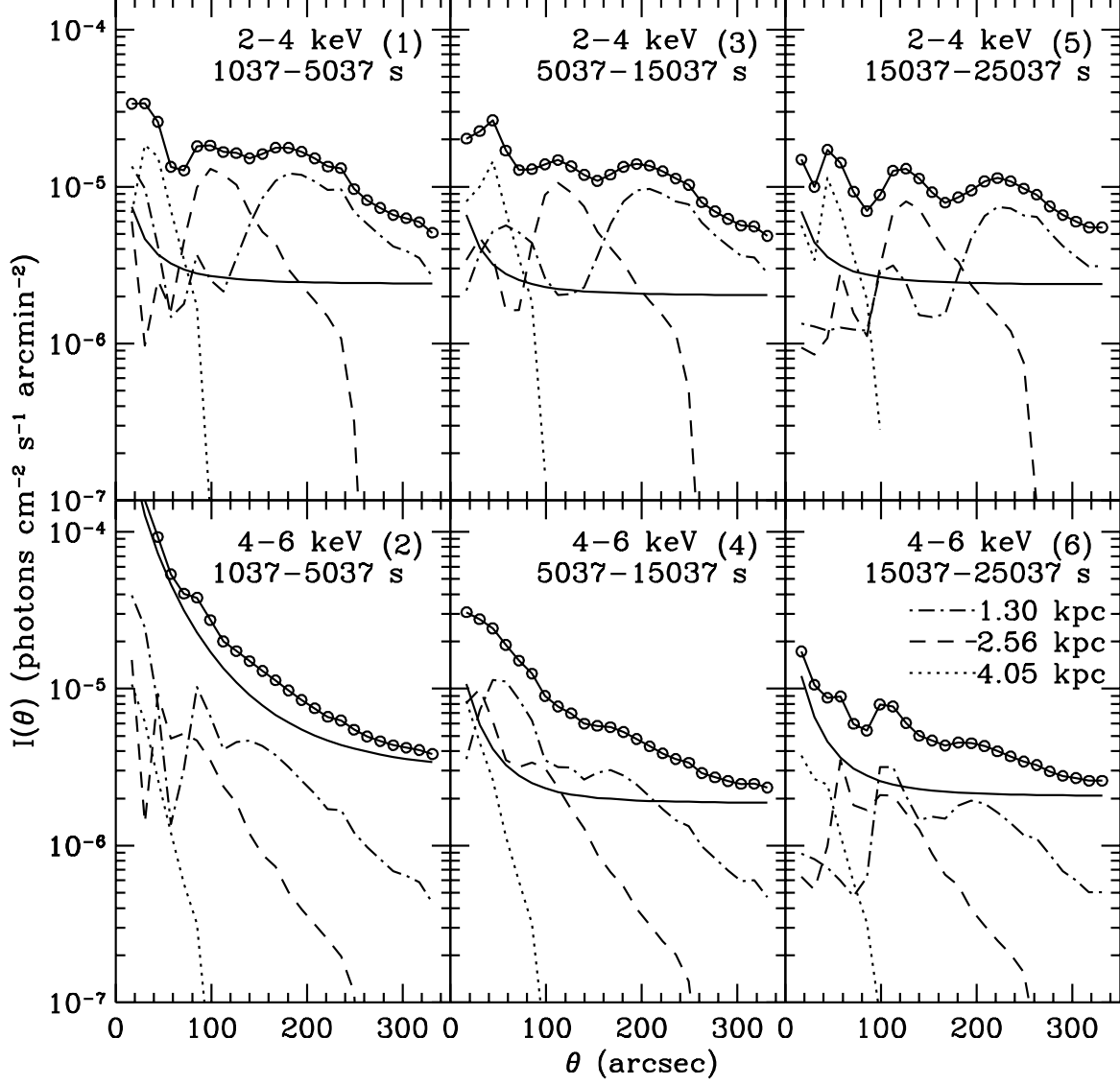


Fig. 12.— Contributions to the simulated halo profiles from scatterings in the three model dust clouds. The line types of the contributions are coded according to the distances of the clouds as indicated in panel (6).

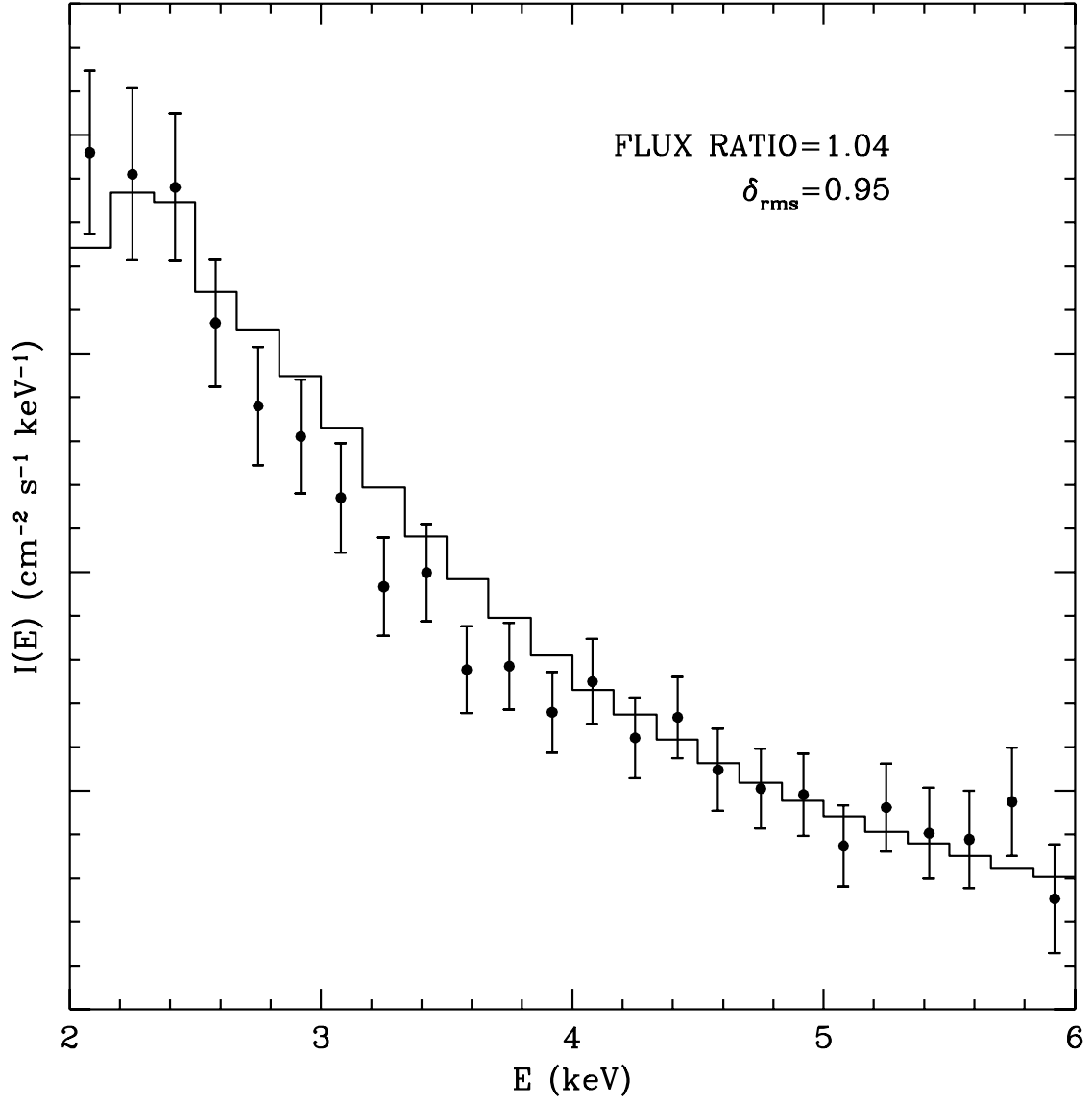


Fig. 13.— Comparison of the spectra of the observed (solid dots) and simulated (histogram) halo in the angle range from $30''$ to $200''$ and time range from 5037 to 25037 s. The rms deviation and the ratio of fluxes in the simulated and observed halos are shown on the plot.

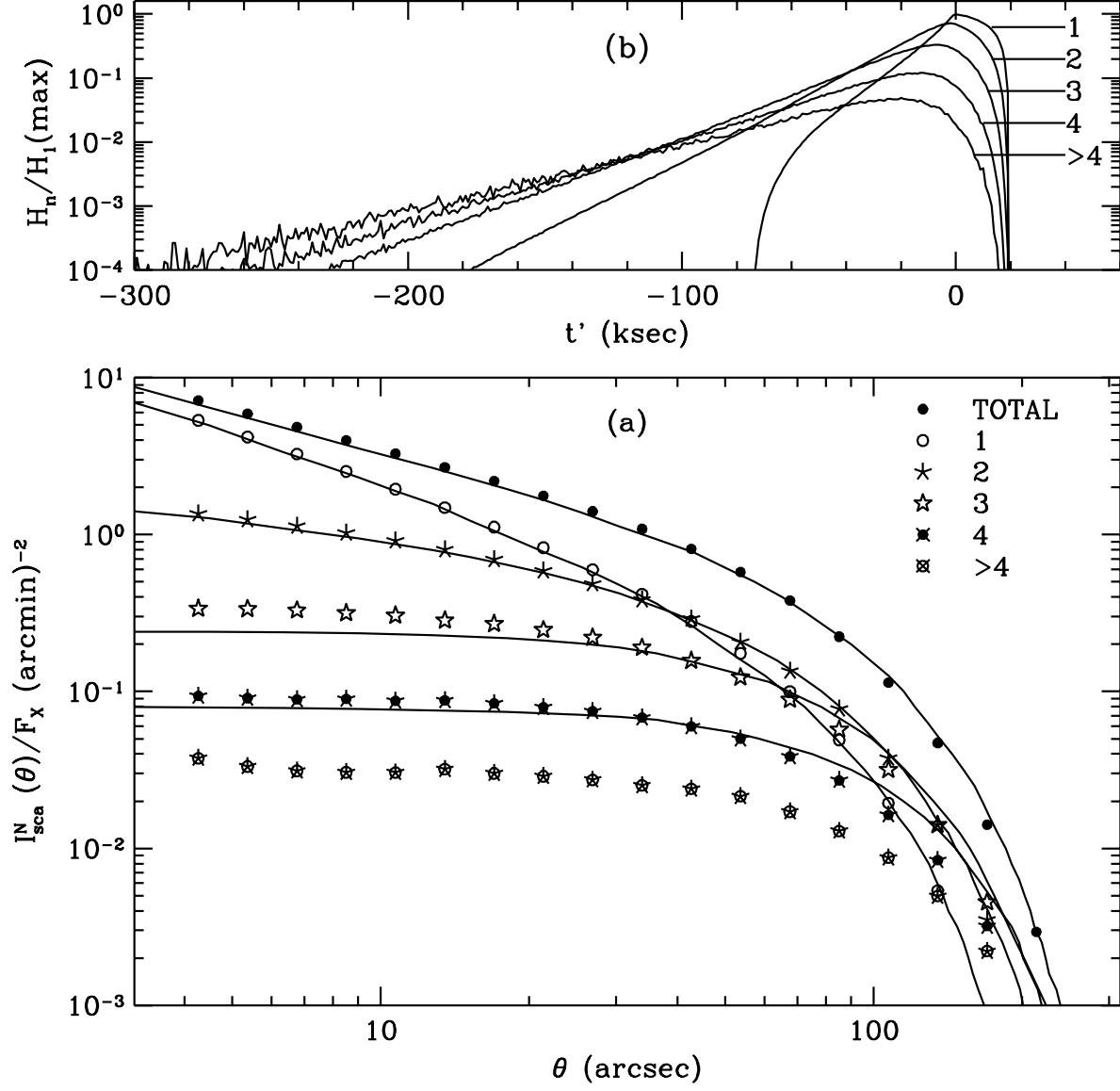


Fig. 14.— (a) Profiles of a simulated halo produced by multiple scattering of 1 keV X-rays by spherical grains with a radius of 1μ distributed uniformly from a source at 7 kpc to the observer with $\tau_{\text{scat}} = 2$. The plotting symbols are coded according to the number of scatterings as indicated. The smooth curves are tracings from the plots of analytical results in Fig. 2 of Mathis & Lee (1991). (b) Relative contributions of trial photons to the multiply scattered halo components plotted against their reduced emission times.

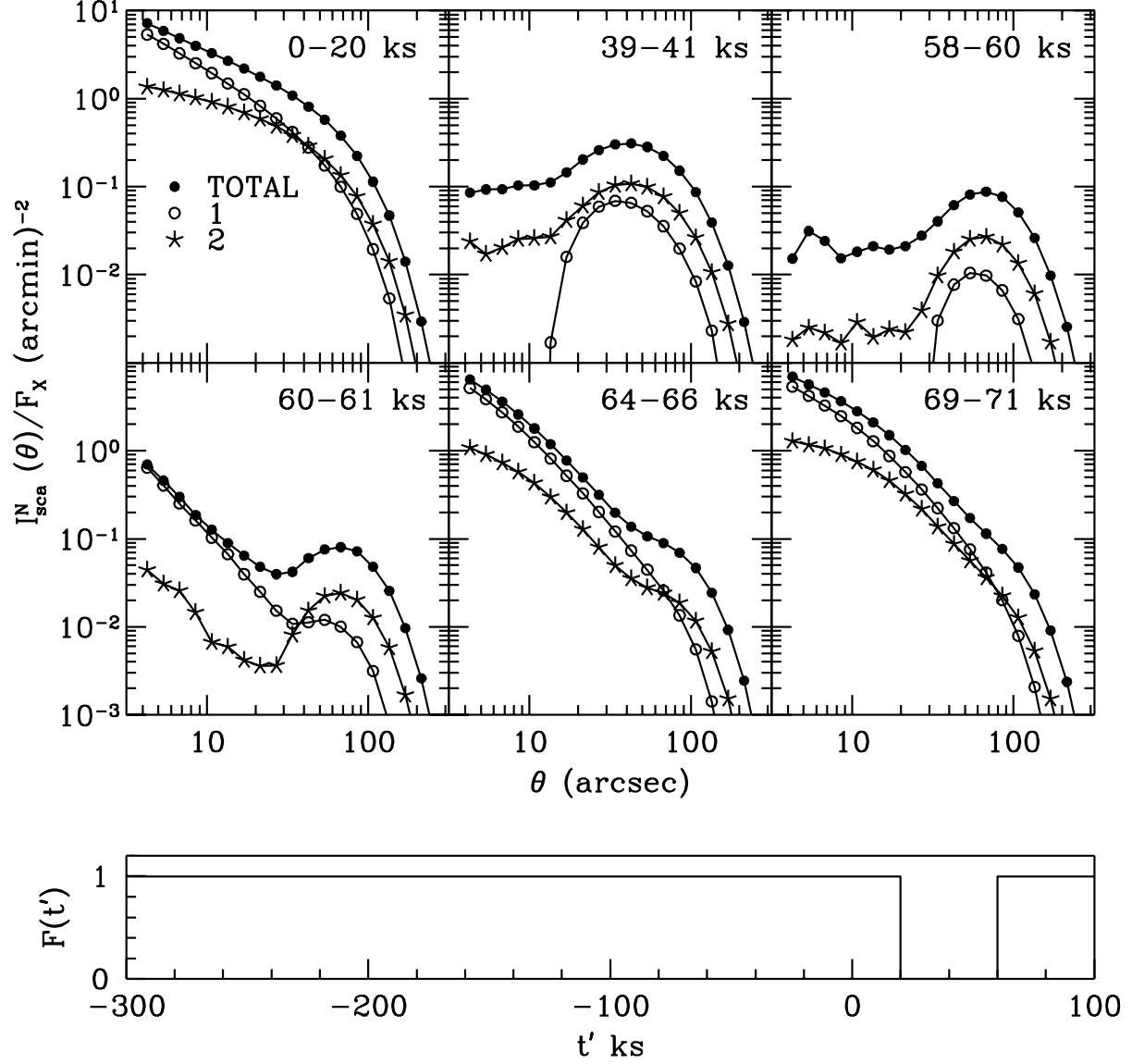


Fig. 15.— Evolution of the simulated halo of Fig. 14 before and after the eclipse immersion at 20 ksec. The flux history is shown in the lower panel. The “observations” centered at 40 ksec and 59 ksec show the gradual hollowing out of the total profile (solid circles) due primarily to the increasing low-angle cutoff of the single scattered component (open circles), but partially filled in by the multiply scattered components (asterisks). The profiles after 60 ksec show the rapid recovery of the profiles after eclipse emersion.